Electronic Supplementary Material (ESI) for Journal of Materials Chemistry A.

Supporting Information

Thermal Convection Induced TiO_2 Microclews as Superior Electrode Materials for Lithium-Ion Batteries

Lijiang Zhao,[a] Shitong Wang, [b] Feng Pan*, [c] Zilong Tang, [b] Zhongtai Zhang,[b] Shengwen Zhong[d] and Junying Zhang*[a]

[a.] Key Laboratory of Micro-nano Measurement, Manipulation and Physics (Ministry of Education), Department of Physics, Beihang University, Beijing 100191, China

[b.] State Key Laboratory of New Ceramics and Fine Processing, School of Materials Science and Engineering, Tsinghua University, Beijing 100084, China

[c.] College of Chemistry and Molecular Engineering, Peking University, Beijing 100871, China

[d.] School of Materials Science and Engineering, Jiangxi University of Science and Technology, Ganzhou 341000, Jiangxi, China

*Corresponding author: chmpf@pku.edu.cn (F. Pan); zjy@buaa.edu.cn (J. Zhang)

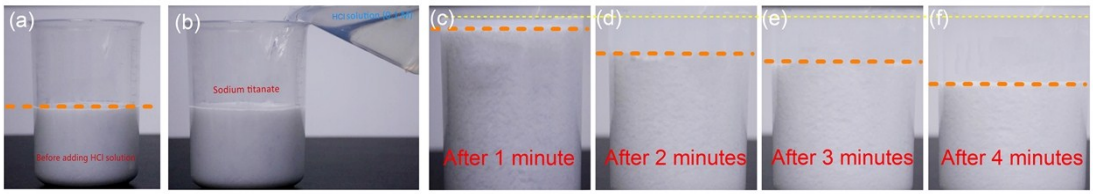

Figure S1. a) The obtained sodium titanate from TCH. b)The process of ion-exchanging. c-f) Settlement state after different times(1,2,3,4 minutes).

We observed the morphology of the samples annealed at 300°C and 400°C as shown in Figure S2. Increasing the annealing temperature caused partially transformation of nanobelt into nanoparticles. This indicates that complete dehydration by high-temperature heating can coarsen the structures.

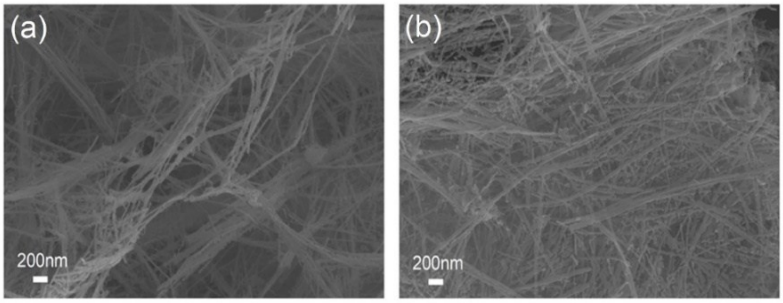

Figure S2. SEM images of the HTO precursor annealing at 300°C (a) and 400°C (b).

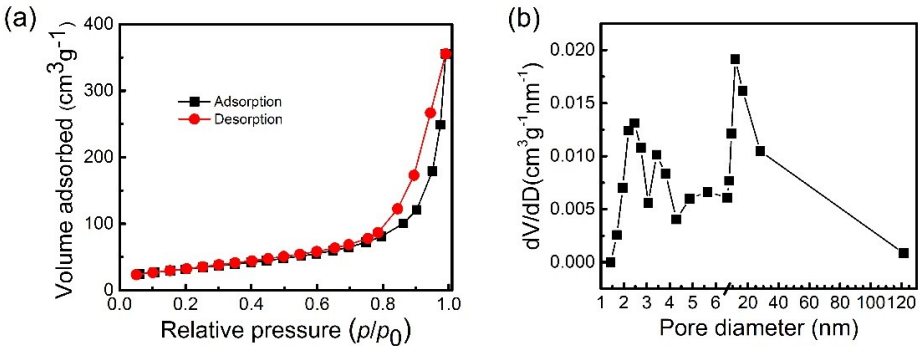

Figure S3. N_2 sorption analysis of TiO_2 MCs samples. a) N_2 adsorption-desorption isotherms of TiO_2 MCs. b) pore-size distribution of TiO_2 MCs.

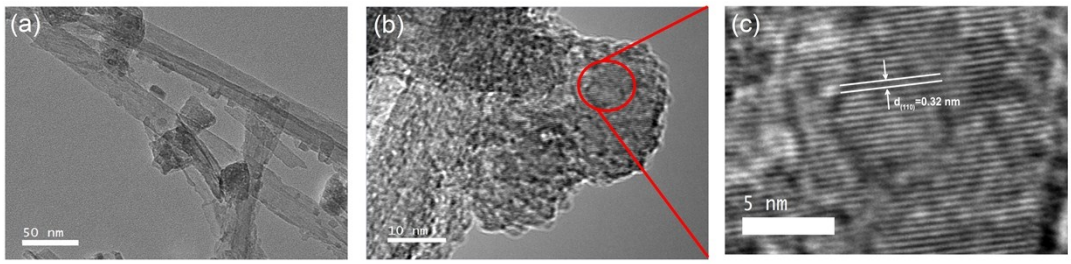

Figure S4. HRTEM of rutile TiO_2 phase in TiO_2 MCs

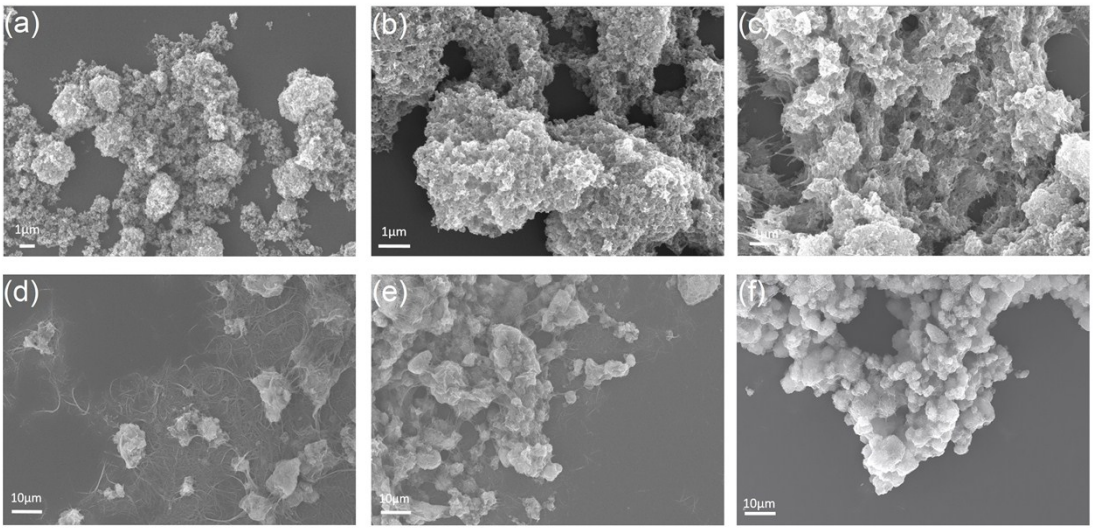

Figure S5. SEM images of the samples prepared under different synthesis time(0 h, 4 h, 8 h, 16 h, 20 h, 24 h).

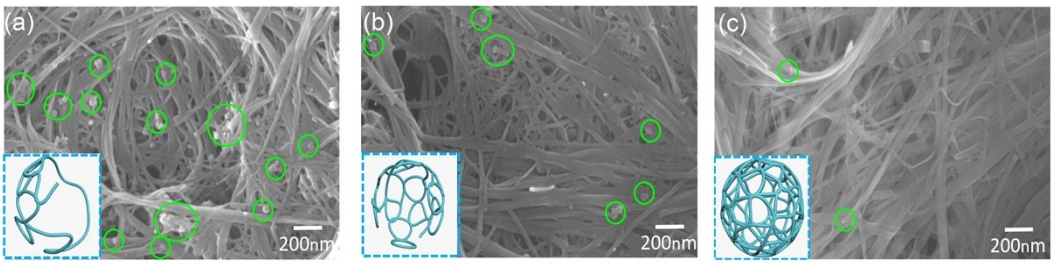

Figure S6. SEM images of the samples under the synthesis time of 16 h (a), 20 h (b) and 24 h (c).The green circles observed on the sample show the dissolution of TiO_2 NPs.

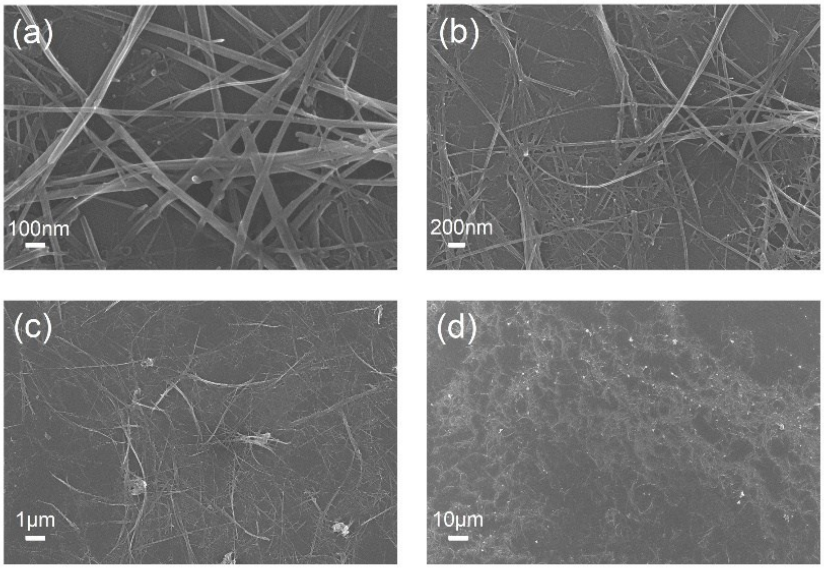

Figure S7. SEM images of the obtained products from uniform heating hydrothermal autoclave accompanied by constant magnetic stirring.

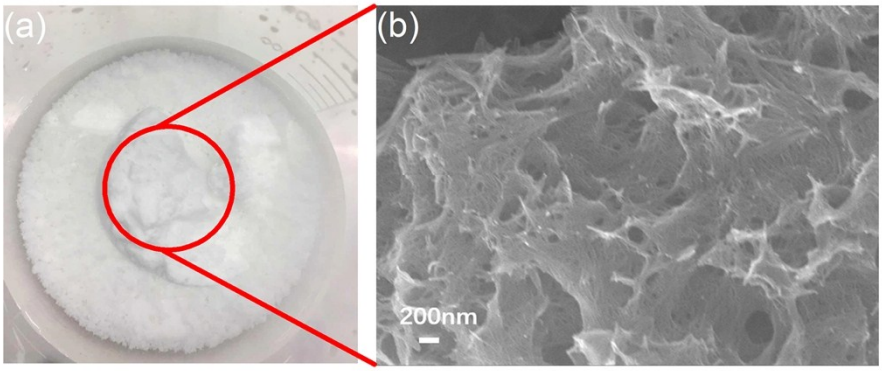

Figure S8. The photo and the SEM image of the obtained HTO from uniformly heated TCH.

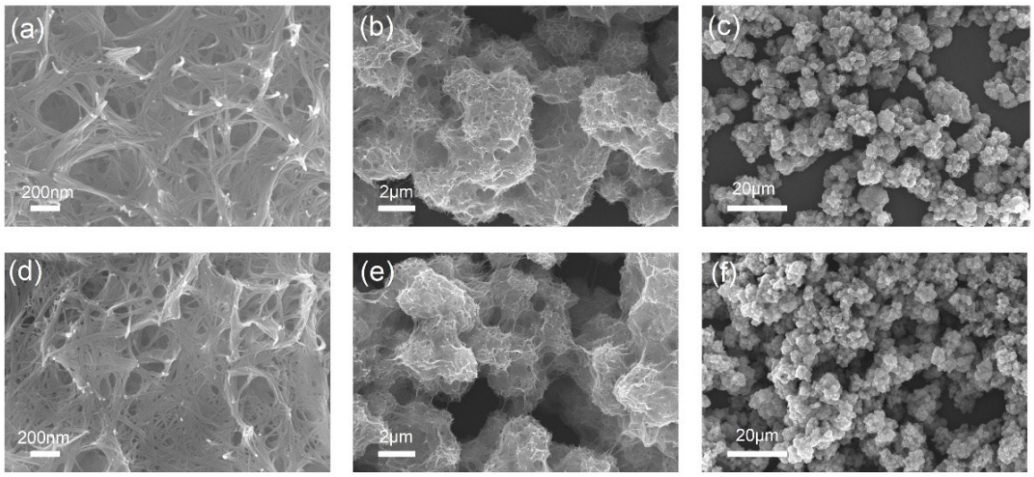

Figure S9. SEM images of the TiO_2 MCs by using commercialized anatase/rutile hybrid TiO_2 (a-c)and commercialized pure anatase TiO_2(d-f)

In order to study the effect of annealing temperature, several samples were synthesized by using different annealing temperatures from ambient temperature to 700 °C and keeping all the other experimental variables fixed. The comparison among these seven electrodes demonstrated the sample prepared at 300 °C could possess the best rate performance (Figure S10).

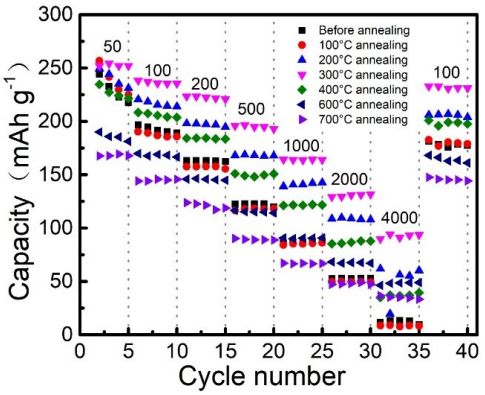

Figure S10. Rate performance of the HTO precursor under the annealing temperature of 100-700 °C by using Al foil collector with the same loading density of 1.2±0.2 mg cm^{-2}. The unit of current density is mA g^{-1}.

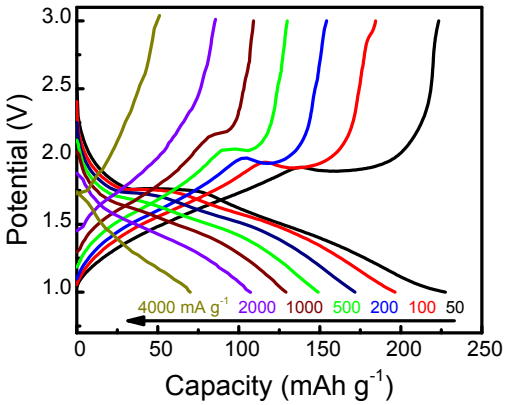

Figure S11. Charge/discharge profiles of TiO_2 MCs@CC electrode.

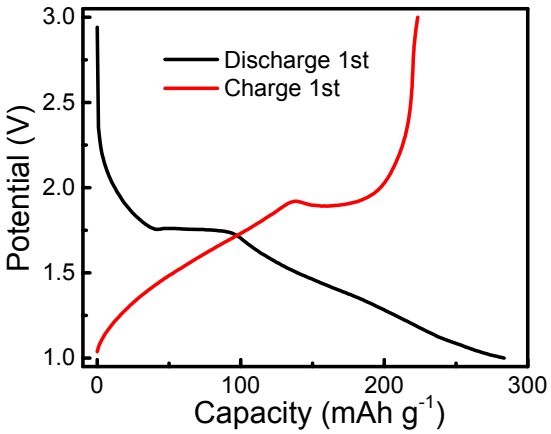

Figure S12. Discharge/charge curves of TiO_2 MCs@CC electrode for the initial cycles in a cut-off voltage window of 1 ~ 3 V at current density of 50 mA g^{-1}.

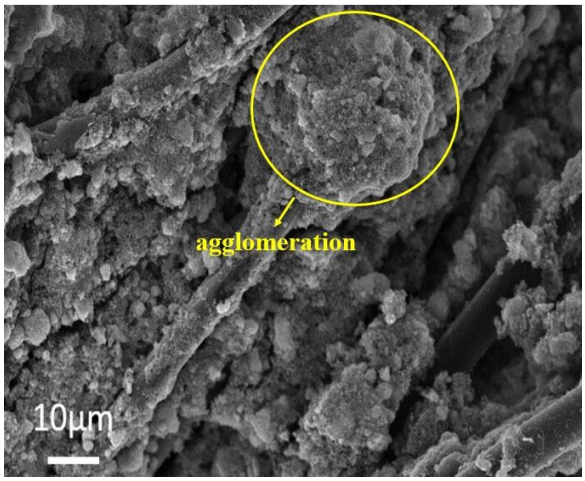

Figure S13. SEM image of TiO_2 NPs@CC electrode.

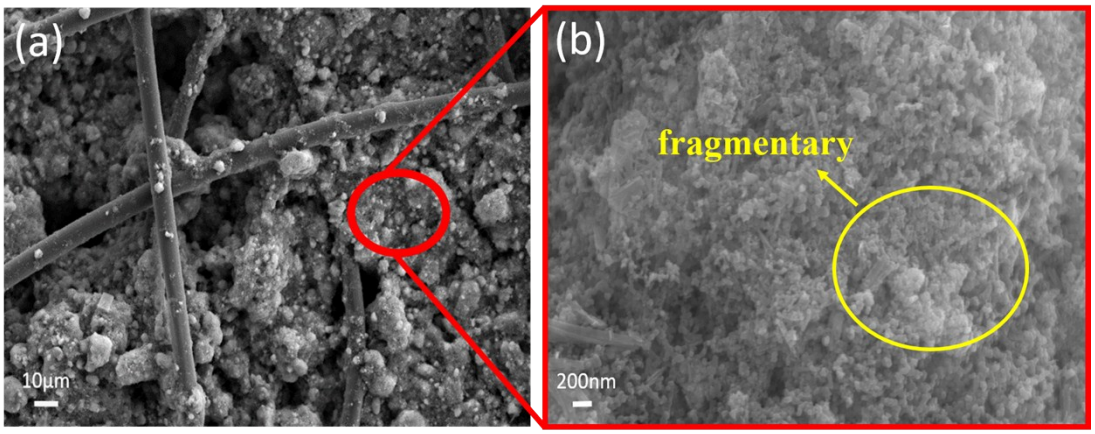

Figure S14. SEM images of TiO_2 MCs-B@CC electrode.

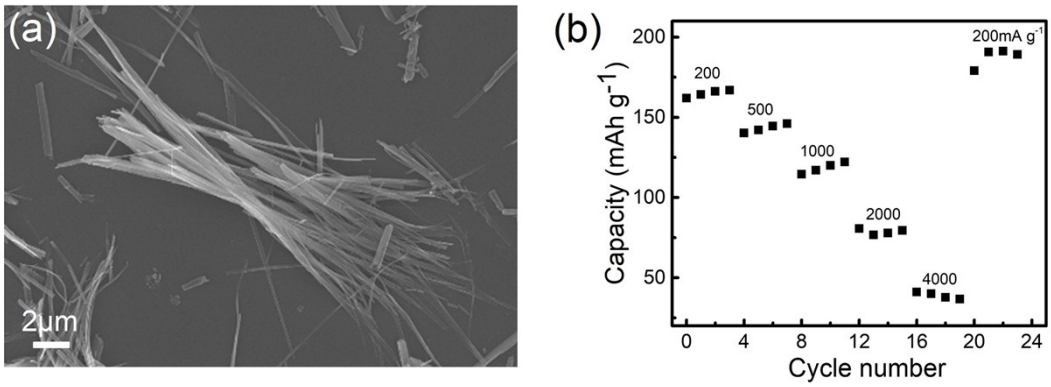

Figure S15. Rate performance of the TiO_2 nanobelts (Synthesis parameters: 400 mg TiO_2 NPs with 10 M NaOH at 180 °C for 48 h) without the clews morphology by using carbon cloth collector with the same loading density of 4 mg cm^{-2}.

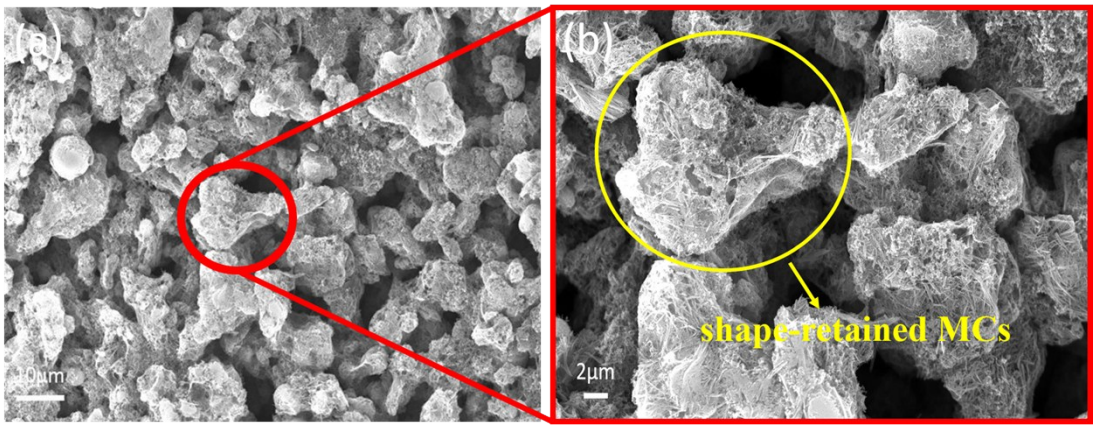

Figure S16. SEM images of TiO_2 MCs@CC electrode.

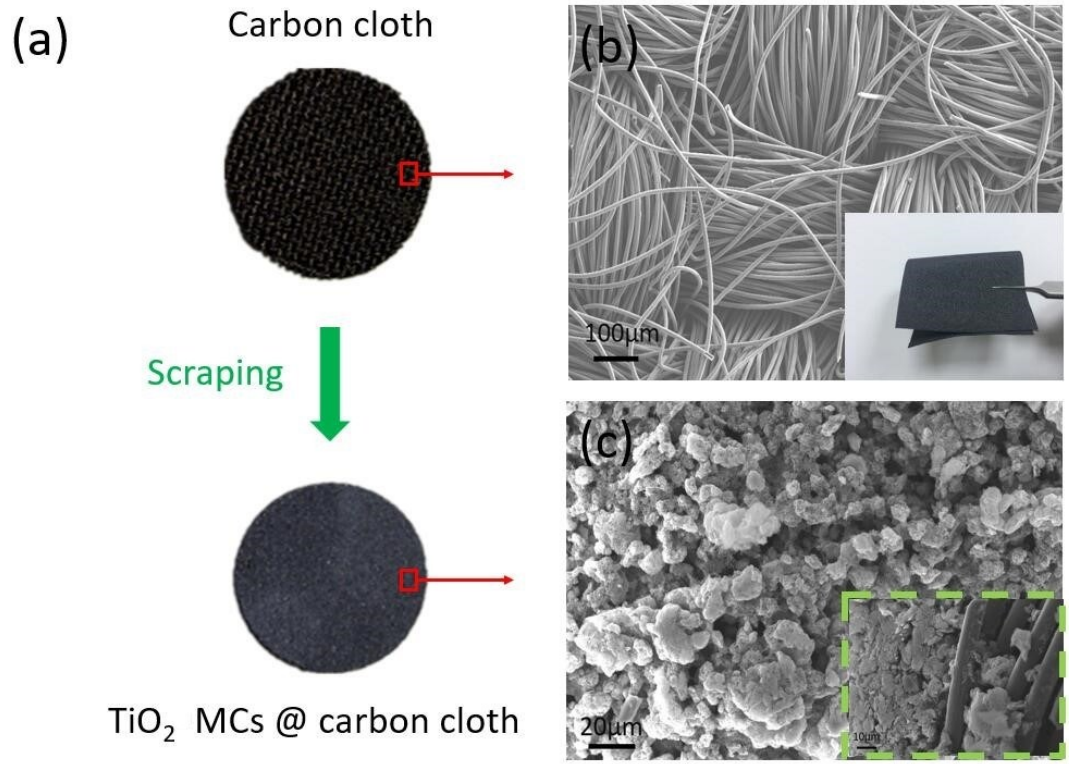

Figure S17. Morphology of the carbon cloth before and after scraper stretching process. a) Digital photos of the carbon cloth before and after scraper stretching process. b) SEM image of the carbon cloth. c) SEM image of the TiO_2 MCs@CC electrode (inset shows the side view of the TiO_2 MCs @CC electrode).

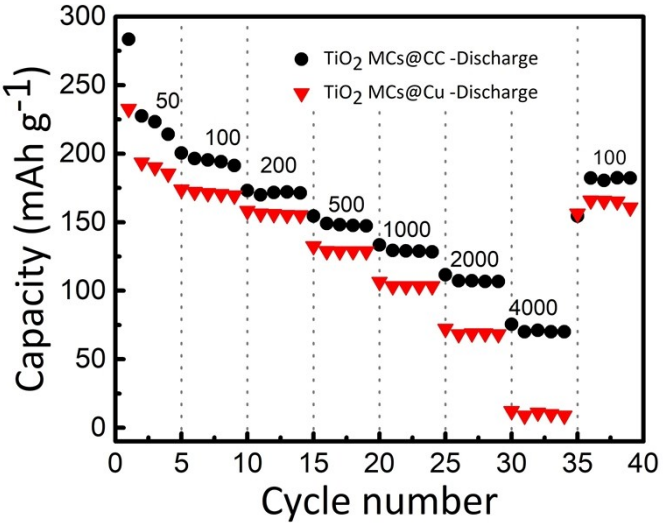

Figure S18 .Rate performance of the TiO_2 MCs@CC and TiO_2 MCs@Cu with the same loading density. The unit of current density is mA g^{-1}.

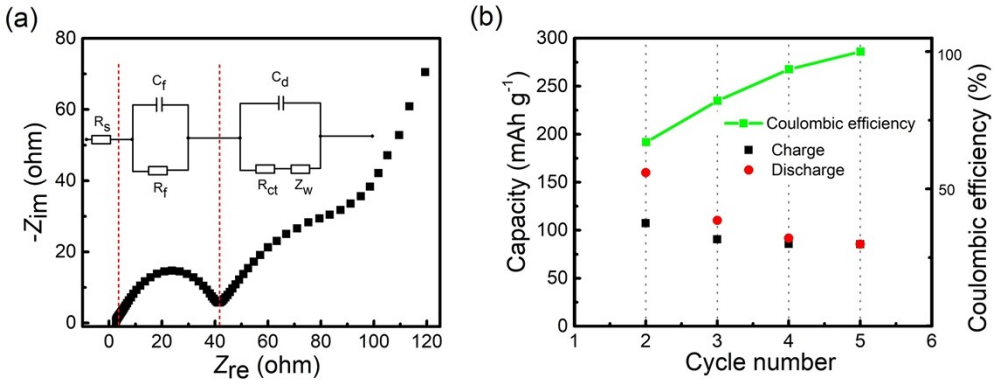

Figure S19. EIS analysis (a) and Coulomb efficiency (b) of TiO_2 NPs @CC electrode.

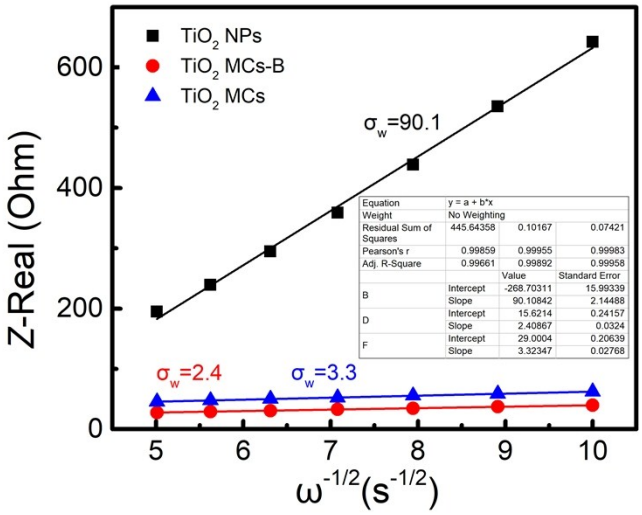

Figure S20. Relationship plot of impedance as a function of the inverse square root of the angular frequency in the Warburg region.

D_{Li} diffusion coefficients calculation

The diffusion coefficients of lithium ions are estimated based on the Warburg diffusion in low frequency using the following equation:

$$D = \frac{R^2T^2}{2A^2F^4n^4C^2\sigma_w^2}$$

wherein R is the gas constant; T is the room absolute temperature; F is the Faraday constant; *A* is the footprint area of the electrode; *n* is the number of electrons involved in the half-reaction for the redox couple; *C* is the molar concentration of lithium ions in a solid; *σ* is the Warburg coefficient which obeys the following relationship:

$$Z' = R_s + R_{ct} + \sigma_w \omega^{-\frac{1}{2}}$$

R, T, and F are constant. *A*, *n*, and *C* remain consistent in the samples of TiO_2 NPs @CC, TiO_2 MCs @CC and TiO_2 MCs-B@CC during tests. Therefore, the $D_{Li} \propto 1/\sigma_w^2$. The D_{Li} diffusion coefficients in TiO_2 MCs @CC and TiO_2 MCs @CC-B are higher than that in the TiO_2 NPs @CC electrode.

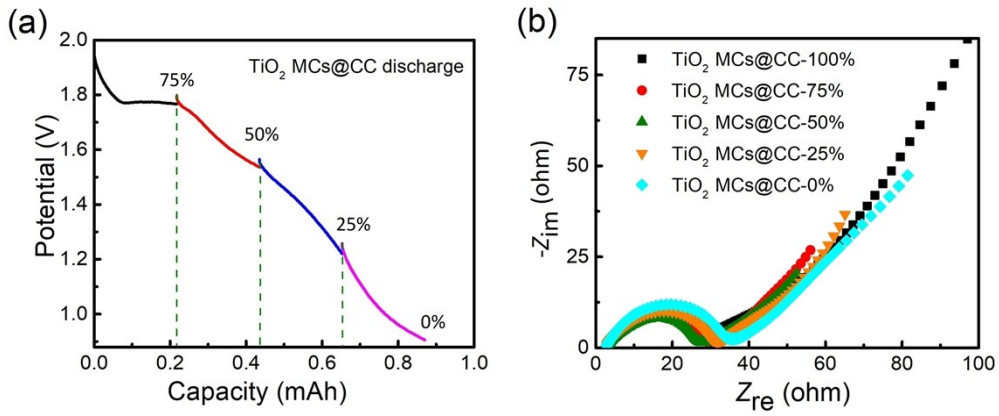

Figure S21. EIS analysis of the TiO_2 MCs@CC electrode under different discharge capacity.

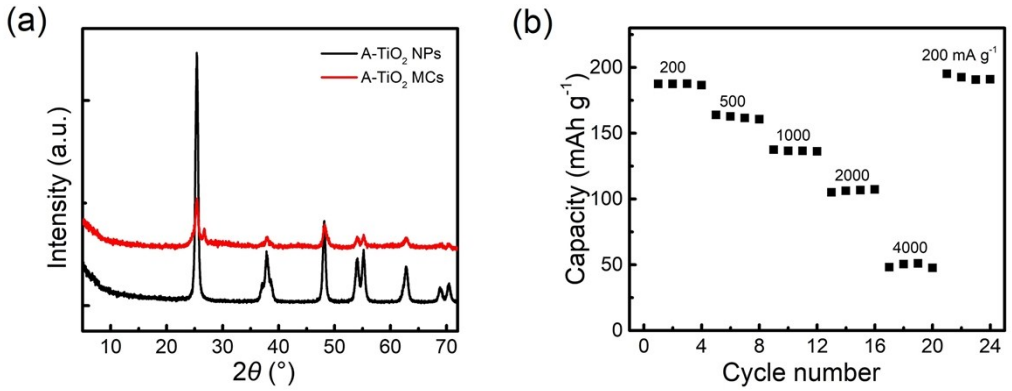

Figure S22. a) XRD of pure anatase TiO_2 NPs (A-TiO_2 NPs) and pure anatase TiO_2 MCs (A-TiO_2 MCs). b) Rate performance of A-TiO_2 MCs with the same loading density (4mg cm^{-2}) on carbon cloth electrode.

Table S1. Comparison of this work with previously reported TiO_2-based high-capacity electrodes.

Materials	loading (mg cm^{-2})	Low rate Performance (mAh g^{-1})	High rate Performance (mAh g^{-1})	References
TiO_2 MCs based carbon cloth	4	171 (200 mA g^{-1})	75 (4000 mA g^{-1}) 110 (2000 mA g^{-1})	this work
TiO_2 inverse opals	0.5-1	196 (75 mA g^{-1})	137 (450 mA g^{-1})	(1)
$Li_4Ti_5O_{12}$/Rutile-TiO_2 Composites	1.8-2	140 (140 mA g^{-1})	80 (1400 mA g^{-1})	(2)
3D $TiO_{2-\delta}$ nanomembranes	0.5	195 (170 mA g^{-1})	107 (1700 mA g^{-1})	(3)
Zinc-Reduced Mesoporous TiO_x	N/A	182 (180 mA g^{-1})	90 (1800 mA g^{-1})	(4)
Three-Dimensional Branched TiO_2 Architectures	0.7	225 (170 mA g^{-1})	150 (1700 mA g^{-1})	(5)
Faceted TiO_2 Crystals	N/A	145 (145 mA g^{-1})	50 (1450 mA g^{-1})	(6)
Crystalline TiO_2 Nanobelts	N/A	220(30 mA g^{-1})	N/A	(7)
TiO_2 ultrathin Nanobelts	N/A	204(197mA g^{-1})	146(1970 mA g^{-1})	(8)

1. D. McNulty, E. Carroll and C. O'Dwyer, *Adv. Energy Mater.*, 2017, **7**, 1602291.
2. P. Wang, G. Zhang, J. Cheng, Y. You, Y. K. Li, C. Ding, J. J. Gu, X. S. Zheng, C. F. Zhang and F. F. Cao, ACS Appl. Mater. Interfaces, 2017, 9, 6138-6143.
3. S. Huang, L. Zhang, X. Lu, L. Liu, L. Liu, X. Sun, Y. Yin, S. Oswald, Z. Zou, F. Ding and O. G. Schmidt, ACS Nano, 2017, 11, 821-830.
4. W. J. Song, S. Yoo, J. I. Lee, J. G. Han, Y. Son, S. I. Kim, M. Shin, S. Choi, J. H. Jang, J. Cho, N. S. Choi and S. Park, Chem Asian J, 2016, 11, 3382-3388.
5. S. Wang, D. Qu, Y. Jiang, W. S. Xiong, H. Q. Sang, R. X. He, Q. Tai, B. Chen, Y. Liu and X. Z. Zhao, ACS Appl. Mater. Interfaces, 2016, 8, 20040-20047.
6. G. Liu, L. C. Yin, J. Pan, F. Li, L. Wen, C. Zhen and H. M. Cheng, Adv. Mater., 2015, 27, 3507-3512.
7. W. Wen, J. M. Wu, Y. Z. Jiang, S. L. Yu, J. Q. Bai, M. H. Cao and J. Cui, Sci Rep, 2015, 5, 11804.
8. P. Gao, D. Bao, Y. Wang, Y. Chen, L. Wang, S. Yang, G. Chen, G. Li, Y. Sun and W. Qin, ACS Appl Mater Interfaces, 2013, 5, 368-373.